

High-Order Accuracy Computation of Coupling Functions for Strongly Coupled Oscillators

Youngmin Park*¹ and Dan Wilson²

¹Department of Mathematics, Brandeis University, Waltham, MA 02453

²Department of Electrical Engineering and Computer Science, University of Tennessee, Knoxville, TN 37996

October 6, 2020

Abstract

We develop a general framework for identifying phase reduced equations for finite populations of coupled oscillators that is valid far beyond the weak coupling approximation. This strategy represents a general extension of the theory from [Wilson and Ermentrout, Phys. Rev. Lett 123, 164101 (2019)] and yields coupling functions that are valid to arbitrary orders of accuracy in the coupling strength. These coupling functions can be used to understand the limiting behavior of potentially high-dimensional, nonlinear coupled oscillators in terms of their phase differences. The proposed formulation accurately replicates nonlinear bifurcations that emerge as the coupling strength increases and is valid in regimes well beyond those that can be considered using classic weak coupling assumptions. We demonstrate the performance of our approach through two examples. First, we use the analytically tractable complex Ginzburg-Landau (CGL) model and demonstrate that our theory accurately predicts bifurcations far beyond the range of existing coupling theory. Second, we use a realistic conductance-based model of a thalamic neuron and show that our theory correctly predicts asymptotic phase differences for non-weak coupling strengths. In both examples, our theory accurately captures model behaviors that existing theories cannot.

1 Introduction

Self-sustained oscillations are observed in a wide array of biological [37, 14], physical [29, 20], and chemical [15, 5] systems. A common and powerful approach to understanding how network oscillators interact is the phase reduction method [15, 14, 9, 22]. Its utility

*Corresponding author. Email ypark@brandeis.edu

comes from reducing a network of N general n -dimensional oscillators into $N - 1$ equations that characterize the temporal evolution of phase differences. Indeed, the weak coupling paradigm has driven much work on coupled oscillators [7, 10, 28, 4, 21, 25] in recent decades.

Unfortunately, the weak coupling assumption cannot be used to accurately capture the dynamical behavior of coupled oscillator networks in many practical applications. This is especially true in many biological applications. For instance, individual cortical neurons elicit small-magnitude postsynaptic responses [13], but the postsynaptic neuron receives tens of thousands of such responses, making synaptic interactions effectively strong [24]. Subcortical networks such as the basal ganglia include strong synaptic conductances [30]. Pacemaker neurons such as those in the pre-Boetzing complex and crab stomatogastric ganglion have coupling strengths several orders of magnitude beyond the regime for which the weak coupling approximation is valid [3, 12]. For weak coupling to serve as a good approximation in these cases, perturbed trajectories must remain within a small neighborhood of the underlying limit cycle – a particularly restrictive requirement for limit cycles that have slowly decaying transients [36, 6].

Recent work has begun to address the fundamental limitations of the weak coupling paradigm. In [35], the authors derive a general second-order correction to the classic first-order theory of weakly coupled oscillators. The method exploits the theory of isostable coordinates [18, 33], which represent level sets of the slowest decaying modes of the Koopman operator [19, 2] to derive the higher-order accuracy corrections for the phase dynamics. The authors in [26, 11] introduce a general numerical method to numerically estimate higher-order phase equations. Finally, although not directly a coupling result, the results of [32] are highly relevant, where Wilson introduced a phase reduction method for strong perturbations using isostable coordinates.

In this paper, we develop a general framework that can be used to identify coupling functions that are valid to arbitrary accuracy in the coupling strength. Related work by [26, 11] requires estimations obtained by the phase dynamics over time, i.e., the full model must be computed for potentially long times and become difficult to implement in high dimensions. In contrast, we exploit the higher-order isostable reduction from [32] and derive high-accuracy phase-interaction functions to arbitrary orders of accuracy in the coupling strength. This work extends upon previous results in [35, 34] that computed second-order accurate coupling functions using the isostable coordinate framework. By restricting our attention to a hypersurface defined by the slowest decaying isostable coordinates, the resulting framework can be readily implemented even if the underlying models are high-dimensional. Furthermore, the numerical implementation only involves computing a hierarchy of scalar ODEs and scalar integrals and does not require *a priori* knowledge of the phase trajectories.

We organize the paper as follows. In Section 2, we introduce our general phase reduction method for N coupled oscillators. In Section 2.1, we demonstrate up to order ε^3 how our symbolic solver derives the reduced equations using $N = 2$ oscillators. We apply our results to the complex Ginzburg-Landau (CGL) ODE model in Section 3.1 and a realistic

conductance-based neural model of a thalamic neuron in Section 3.2. We conclude with a discussion in Section 4.

All code used to generate the phase equations are publicly available on GitHub at <https://github.com/youngmp/strongcoupling>. Our open-source implementation is written in Python [31]. The repository includes documentation on how to use our software for general systems including additional examples.

2 Derivation

In this section, we reduce the dynamics of N strongly coupled oscillators to a system of $N - 1$ equations representing the phase differences. We begin with the autonomous ODEs

$$\dot{X}_i = F(X_i) + \varepsilon \sum_{j=1}^N a_{ij} G(X_i, X_j), \quad i = 1, \dots, N, \quad (1)$$

where each system admits a T -periodic limit cycle $Y(t)$ when $\varepsilon = 0$. We allow $\varepsilon > 0$ not necessarily small and assume general smooth vector fields $F : \mathbb{R}^n \rightarrow \mathbb{R}^n$ and a smooth coupling function $G : \mathbb{R}^n \times \mathbb{R}^n \rightarrow \mathbb{R}^n$. The scalars a_{ij} modulate the strength of coupling between pairs of oscillators, whereas ε modulates the overall coupling strength of the network. Throughout the text, we will use subscripts i and j to denote oscillator indices and superscripts k and ℓ to denote exponents and expansions.

Similar to prior studies [33, 35], we make the explicit assumption that all but one of the $n - 1$ non-unity Floquet multipliers is sufficiently close to 0 so that only a single isostable coordinate is required per oscillator. Additional isostable coordinates could be considered with appropriate modifications to the derivation to follow. Let $\kappa < 0$ be the corresponding Floquet exponent. Using the theory of isostable reduction [35, 32], Equation (1) reduces to the phase-amplitude coordinates,

$$\begin{aligned} \dot{\theta}_i &= 1 + \varepsilon \mathcal{Z}(\theta_i, \psi_i) \cdot \sum_{j=1}^N a_{ij} G(\theta_i, \theta_j), \\ \dot{\psi}_i &= \kappa \psi_i + \varepsilon \mathcal{I}(\theta_i, \psi_i) \cdot \sum_{j=1}^N a_{ij} G(\theta_i, \theta_j). \end{aligned} \quad (2)$$

where θ_i represents the phase of oscillator i and ψ_i represents the amplitude of a trajectory perturbed away from the underlying limit cycle. The functions \mathcal{Z} and \mathcal{I} can be computed

to arbitrarily high accuracy by computing coefficients of the expansions:

$$\mathcal{Z}(\theta, \psi) \approx Z^{(0)}(\theta) + \psi Z^{(1)}(\theta) + \psi^2 Z^{(2)}(\theta) + \dots, \quad (3)$$

$$\mathcal{I}(\theta, \psi) \approx I^{(0)}(\theta) + \psi I^{(1)}(\theta) + \psi^2 I^{(2)}(\theta) + \dots, \quad (4)$$

$$X_i(t) \approx Y(\theta_i) + \psi_i g^{(1)}(\theta_i) + \psi_i^2 g^{(2)}(\theta_i) + \dots, \quad (5)$$

$$\psi_i(t) \approx \varepsilon p_i^{(1)}(t) + \varepsilon^2 p_i^{(2)}(t) + \varepsilon^3 p_i^{(3)}(t) + \dots, \quad (6)$$

where $Z^{(k)}$, $I^{(k)}$, and $g^{(k)}$ are the PRC, IRC, and Floquet eigenfunction expansions respectively, θ_i are the phase variables of each oscillator and ψ_i are the amplitude coordinates. Using the method in [32], these functions can be computed numerically provided the underlying equations are known. We will assume that we have performed such computations for a given system and have solutions $Z^{(k)}$, $I^{(k)}$, and $g^{(k)}$ for each k (our Python implementation includes methods that automate the computation of these functions).

Next, we expand the coupling function G in powers of ε . Let us fix a particular pair of oscillators i and j . To expand G in powers of ε , we use the Floquet eigenfunction approximation

$$\Delta x_i \approx \psi_i g^{(1)}(\theta_i) + \psi_i^2 g^{(2)}(\theta_i) + \dots, \quad (7)$$

where $\Delta x_i \equiv X_i(t) - Y(\theta_i)$. We view the coupling function as the map $G : \mathbb{R}^{2n} \rightarrow \mathbb{R}^n$ where $G(X) = [G_1, \dots, G_n]^T \in \mathbb{R}^n$, $G_k : \mathbb{R}^{2n} \rightarrow \mathbb{R}$, and $X = [X_i^T, X_j^T]^T \in \mathbb{R}^{2n}$. We then apply the standard definition of higher-order derivatives from [17, 32] to obtain the multivariate Taylor expansion in Δx_i .

Starting with $G(Y + \Delta X)$, where $Y = [Y(\theta_i)^T, Y(\theta_j)^T]^T$, and $\Delta X = [\Delta x_i^T, \Delta x_j^T]^T$, the Taylor expansion yields

$$G_i(Y + \Delta X) = G_i(Y) + G_i^{(1)}(Y) \Delta X + \sum_{k=2}^{\infty} \frac{1}{k!} \left[\otimes \Delta X^T \right] \text{vec} \left(G_i^{(k)}(Y) \right), \quad (8)$$

where

$$G_i^{(k)} = \frac{\partial \text{vec} \left(G_i^{(k-1)} \right)}{\partial X^T} \in \mathbb{R}^{n^{(k-1)} \times n}. \quad (9)$$

That is, the partial of G is taken with respect to all coordinates of oscillators i and j . We replace ΔX in Equation (9) with the Floquet eigenfunction expansions (Equation (7)) and replace each ψ_i^k with the expansion for ψ_i (Equation (6)). With these substitutions in place, we collect the expansion of G in powers of ε . In general, the notation becomes cumbersome, so we summarize this step by writing

$$G(\theta_i, \theta_j) = K^{(0)}(\theta_i, \theta_j) + \varepsilon K^{(1)}(\theta_i, \theta_j) + \varepsilon^2 K^{(2)}(\theta_i, \theta_j) + \dots \quad (10)$$

The $K^{(k)}$ functions are the appropriately-collected terms including partials of G and the Floquet eigenfunctions. Our Python implementation includes methods that automate the collection of these terms.

At this step, we have all the necessary expansions in ε to rewrite the phase-amplitude equations in Equation (2) in powers of ε . However, this system is still in two dimensions per oscillator. In order to reduce the equations to one per oscillator, we solve for ψ_i in terms of θ_i, θ_j . To this end, we proceed with the method suggested by [35].

Making the substitution $\hat{\theta}_i = \theta_i - t$ in Equation (2) yields,

$$\dot{\hat{\theta}}_i = \varepsilon \sum_{j=1}^N a_{ij} \mathcal{Z}(\hat{\theta}_i + t, \psi_i) \cdot G(\hat{\theta}_i + t, \hat{\theta}_j + t), \quad (11)$$

$$\dot{\psi}_i = \kappa \psi_i + \varepsilon \sum_{j=1}^N a_{ij} \mathcal{I}(\hat{\theta}_i + t, \psi_i) \cdot G(\hat{\theta}_i + t, \hat{\theta}_j + t). \quad (12)$$

Now substituting the expansion $\psi_i(t) = \varepsilon p_i^{(1)}(t) + \varepsilon^2 p_i^{(2)}(t) + \varepsilon^3 p_i^{(3)}(t) + \dots$, into Equation (12), yielding a hierarchy of ODEs in powers of ε of ψ_i in terms of $\hat{\theta}_i, \hat{\theta}_j$. The left-hand side consists of straightforward time-derivatives:

$$\psi_i' = \varepsilon \frac{d}{dt} p_i^{(1)} + \varepsilon^2 \frac{d}{dt} p_i^{(2)} + \varepsilon^3 \frac{d}{dt} p_i^{(3)} + \dots$$

The right-side, after plugging in the function expansions, reads

$$\begin{aligned} & \kappa \psi_i + \varepsilon \sum_{j=1}^N a_{ij} \mathcal{I}(\hat{\theta}_i + t, \psi_i) \cdot G(\hat{\theta}_i + t, \hat{\theta}_j + t) \\ &= \kappa \left[\varepsilon p_i^{(1)}(t) + \varepsilon^2 p_i^{(2)}(t) + \dots \right] \\ &+ \varepsilon \sum_{j=1}^N a_{ij} \left(\left[I_i^{(0)}(\hat{\theta}_i + t) + \psi I_i^{(1)}(\hat{\theta}_i + t) + \psi^2 I_i^{(2)}(\hat{\theta}_i + t) + \dots \right] \right. \\ &\quad \left. \cdot \left[K_i^{(0)}(\hat{\theta}_i + t, \hat{\theta}_j + t) + \varepsilon K_i^{(1)}(\hat{\theta}_i + t, \hat{\theta}_j + t) + \varepsilon^2 K_i^{(2)}(\hat{\theta}_i + t, \hat{\theta}_j + t) + \dots \right] \right). \end{aligned}$$

These expansions yield the hierarchy of scalar ODEs in ε ,

$$\begin{aligned}
O(\varepsilon) : \quad & \frac{dp_i^{(1)}}{dt} = \kappa p_i^{(1)}(t) + \sum_{j=1}^N a_{ij} I^{(0)} \cdot K^{(0)}, \\
O(\varepsilon^2) : \quad & \frac{dp_i^{(2)}}{dt} = \kappa p_i^{(2)} + \sum_{j=1}^N a_{ij} \left(I^{(0)} \cdot K^{(1)} + p_i^{(1)} I^{(1)} \cdot K^{(0)} \right), \\
O(\varepsilon^3) : \quad & \frac{dp_i^{(3)}}{dt} = \kappa p_i^{(3)} + \sum_{j=1}^N a_{ij} \left(I^{(0)} \cdot K^{(2)} + p_i^{(1)} I^{(1)} \cdot K^{(1)} \right. \\
& \quad \left. + p_i^{(2)} I^{(1)} \cdot K^{(0)} + \left(p_i^{(1)} \right)^2 I^{(2)} \cdot K^{(0)} \right), \\
& \quad \vdots
\end{aligned}$$

where $p_i^{(k)}$ are functions of time t (with phase shifts in $\hat{\theta}_i$ and $\hat{\theta}_j$ as we will show below), $I^{(k)}$ are functions of $\hat{\theta}_i + t$, and $K^{(k)}$ are functions of $\hat{\theta}_i + t, \hat{\theta}_j + t$. Note that all ODEs are first-order inhomogeneous differential equations with forcing terms that depend on lower-order solutions, so we can solve each ODE explicitly.

Let $f^{(k)}(\hat{\theta}_i + t, \hat{\theta}_j + t)$ be the forcing function of the ODE for order $O(\varepsilon^k)$. The integrating factor method yields,

$$p_i^{(k)}(t) = \sum_{j=1}^N a_{ij} \int_0^t e^{\kappa(t-s)} f^{(k)}(\hat{\theta}_i + s, \hat{\theta}_j + s) ds + e^{\kappa t} C, \quad j = 1, 2, \dots$$

where C is a constant of integration. To discard transients, we ignore the constant of integration and set the lower bound of the integral to $-\infty$. For convenience, we also make the change of variables $s \rightarrow t - s$. The solutions then become,

$$p_i^{(k)}(t) = \sum_{j=1}^N a_{ij} \int_0^\infty e^{\kappa s} f^{(k)}(\hat{\theta}_i + t - s, \hat{\theta}_j + t - s) ds \quad (13)$$

$$\equiv p_i^{(k)}(\hat{\theta}_1 + t, \dots, \hat{\theta}_N + t). \quad (14)$$

Recalling that $p_i^{(k)}$ are coefficients of the ε -expansion of ψ_i , it follows that each ψ_i can be written in terms of $\hat{\theta}_1, \dots, \hat{\theta}_N$ (note the lowest order $p_i^{(k)}$ is the same function as the function r_j as [35]). We now substitute the expansion for ψ_i into Equation (11). Again, in general, the notation becomes cumbersome, so we proceed without explicitly writing the expansions. Our Python implementation also automates this process, and we will show an example of how this process is done in the next section.

Because $\mathcal{Z}(\hat{\theta}_i, \psi_i)$ is a function of $p_i^{(k)}$, we write $\mathcal{Z}(\hat{\theta}_i, \psi_i) = \mathcal{Z}(\hat{\theta}_1 + t, \dots, \hat{\theta}_N + t)$, transform Equation (11) using $s = \theta_i + t$, and average it to yield:

$$\dot{\theta}_i = \frac{\varepsilon}{T} \sum_{j=1}^N a_{ij} \int_0^T \mathcal{Z}(\theta_1 - \theta_i + s, \dots, \theta_N - \theta_i + s) \cdot G(s, \theta_j - \theta_i + s) ds. \quad (15)$$

Averaging is a reasonable assumption because we generally expect the phase differences $\theta_i - \theta_j$ to be slow relative to the timescale of oscillations. This system of equations represent the phase dynamics of N strongly coupled oscillators taking into account the amplitude dynamics. Finally, to write the phase difference equation, we define $\phi_i = \theta_i - \theta_1$, yielding the scalar equations,

$$\begin{aligned} \dot{\phi}_i = & \varepsilon \sum_{j=1}^N a_{ij} \mathcal{H}(-\phi_i, \phi_2 - \phi_i, \dots, \phi_N - \phi_i, \phi_j - \phi_i) \\ & - \varepsilon \sum_{j=1}^N a_{ij} \mathcal{H}(0, \phi_2, \dots, \phi_N, \phi_j), \quad i = 2, \dots, N, \end{aligned}$$

where

$$\mathcal{H}(\eta_1, \dots, \eta_N, \xi) = \frac{1}{T} \int_0^T \mathcal{Z}(\eta_1 + s, \dots, \eta_N + s) \cdot G(s, \xi + s) ds.$$

We have reduced a system of N arbitrarily general n -dimensional oscillators into a system of $N - 1$ scalar equations, concluding the derivation. We call \mathcal{H} the generalized interaction function, because it closely resembles the interaction function from the classic theory of weakly coupled oscillators. Just as in the classic theory, the existence and stability of fixed points of this system correspond to phase-locked states in the full oscillator system.

In practice, our Python implementation views \mathcal{H} as an expansion in powers of ε :

$$\varepsilon \mathcal{H} = \varepsilon \mathcal{H}^{(1)} + \varepsilon^2 \mathcal{H}^{(2)} + \dots,$$

and computes each $\mathcal{H}^{(k)}$ up to the desired order. An explicit example using two oscillators up to order ε^3 is shown below. The choice of truncation depends on the desired accuracy, on the magnitude of ε , and on the system under consideration. High-dimensional systems add to the computational difficulty, but the dimensionality does not necessarily pose the greatest bottleneck when applying this method.

We note that for numerical implementation, computing Equation (13) is the most computationally expensive step because it a scalar time integral that must be recomputed for pairs of phase variables. We refer the reader to Appendix A for details of our numerical approach.

2.1 Computation of Coupling Functions for $N = 2$ Oscillators

As a concrete example of how our symbolic script generates phase equations, we show the process for deriving the phase equations for two reciprocally coupled oscillators θ_1, θ_2 up to order $O(\varepsilon^3)$. We assume a system of $N = 2$ coupled oscillators without self-coupling ($a_{ii} = 0$). We write $\eta_i = \hat{\theta}_i + t$ for brevity.

Recall the ε -expansion in the coupling function G in the previous section:

$$G(\eta_1, \eta_2) = K^{(0)}(\eta_1, \eta_2) + \varepsilon K^{(1)}(\eta_1, \eta_2) + \varepsilon^2 K^{(2)}(\eta_1, \eta_2) + O(\varepsilon^3).$$

Each $K^{(k)}$ contains the amplitude expansions ψ_1 and ψ_2 , which are quantities that must be made explicit for this example. To this end, we derive more explicit forms for $K^{(k)}$ by plugging in the Floquet eigenfunction expansions

$$\Delta x_i \approx \psi_i(t)g^{(1)}(\eta_i) + \psi_i^2 g^{(2)}(\eta_i) + O(\psi_i^3),$$

into the derivative expansion of G ,

$$G_i(Y + \Delta X) = G_i(Y) + G_i^{(1)}(Y)\Delta X + \sum_{k=2}^{\infty} \frac{1}{k!} \left[\otimes \Delta X^T \right] \text{vec} \left(G_i^{(k)}(Y) \right),$$

and collect in powers of ψ_i . The appropriately-collected terms are

$$G(\eta_1, \eta_2) = \sum_{k+\ell \leq 2} \psi_1^k(t)\psi_2^\ell(t)M^{(k,\ell)}(\eta_1, \eta_2), \quad (16)$$

where the functions $M^{(k,\ell)}$ are maps $M^{(k,\ell)} : S^1 \times S^1 \rightarrow \mathbb{R}^2$ consisting of the expanded Floquet eigenfunctions of order $\psi^k\psi^\ell$ and the partial derivatives of G . To obtain an expansion in ε , we plug in the amplitude expansion (Equation (6)) and collect in powers of ε , noting that for $N = 2$ without self coupling, the $p_i^{(k)}(t)$ terms are

$$\begin{aligned} p_i^{(k)}(t) &= \int_0^\infty e^{\kappa s} f^{(k)}(\hat{\theta}_i + t - s, \hat{\theta}_j + t - s) ds \\ &\equiv p_i^{(k)}(\hat{\theta}_i + t, \hat{\theta}_j + t), \end{aligned}$$

where $i = 1, 2, j = 3 - i$. The resulting $K^{(k)}$ functions are,

$$\begin{aligned} K^{(0)}(\eta_1, \eta_2) &= M^{(0,0)}(\eta_1, \eta_2), \\ K^{(1)}(\eta_1, \eta_2) &= p_2^{(1)}(\eta_2, \eta_1)M^{(0,1)}(\eta_1, \eta_2) + p_1^{(1)}(\eta_1, \eta_2)M^{(1,0)}(\eta_1, \eta_2), \\ K^{(2)}(\eta_1, \eta_2) &= \left(p_2^{(1)}(\eta_2, \eta_1) \right)^2 M^{(0,2)}(\eta_1, \eta_2) + p_1^{(1)}(\eta_1, \eta_2)p_2^{(1)}(\eta_2, \eta_1)M^{(1,1)}(\eta_1, \eta_2), \\ &\quad + \left(p_1^{(1)}(\eta_1, \eta_2) \right)^2 M^{(2,0)}(\eta_1, \eta_2). \end{aligned}$$

Next, we write the ε -expansion of the PRC function \mathcal{Z} , again using the amplitude expansion (Equation (6)):

$$\begin{aligned}\mathcal{Z}(\eta_1) &= Z^{(0)}(\eta_1) + \varepsilon p_1^{(1)}(\eta_1, \eta_2) Z^{(1)}(\eta_1) \\ &\quad + \varepsilon^2 \left[p_1^{(2)}(\eta_1, \eta_2) Z^{(1)}(\eta_1) + \left(p_1^{(1)}(\eta_1, \eta_2) \right)^2 Z^{(2)}(\eta_1) \right] + O(\varepsilon^3),\end{aligned}$$

where $i = 1, 2, j = 3 - i$. We now plug the ε -expansions for G and \mathcal{Z} into the phase equation, Equation (11), and average to yield,

$$\theta_1 = \varepsilon \mathcal{H}^{(1)}(\theta_2 - \theta_1) + \varepsilon^2 \mathcal{H}^{(2)}(\theta_2 - \theta_1) + \varepsilon^3 \mathcal{H}^{(3)}(\theta_2 - \theta_1) + O(\varepsilon^4),$$

where

$$\begin{aligned}\mathcal{H}^{(1)}(\eta) &= \frac{1}{T} \int_0^T Z^{(0)} \cdot M^{(0,0)} ds. \\ \mathcal{H}^{(2)}(\eta) &= \frac{1}{T} \int_0^T p_1^{(1)} Z^{(1)} \cdot M^{(0,0)} + p_2^{(1)} Z^{(0)} \cdot M^{(0,1)} + p_1^{(1)} Z^{(0)} M^{(1,0)} ds. \\ \mathcal{H}^{(3)}(\eta) &= \frac{1}{T} \int_0^T \left[p_1^{(2)} Z^{(1)} \cdot M^{(0,0)} + \left(p_1^{(1)} \right)^2 Z^{(2)} \cdot M^{(0,0)} \right. \\ &\quad \left. + p_1^{(1)} p_2^{(1)} Z^{(1)} \cdot M^{(0,1)} + \left(p_1^{(1)} \right)^2 Z^{(1)} \cdot M^{(1,0)} \right] ds.\end{aligned}$$

All $Z^{(k)}$ are functions of the integrating variable s , all $M^{(k,\ell)}$ are functions of $(s, \eta + s)$, all $p_1^{(k)}$ are functions of $(s, \eta + s)$, and all $p_2^{(k)}$ are functions of $(\eta + s, s)$. The equation for θ_2 is identical, but with $\theta_1 - \theta_2$ as inputs to the $\mathcal{H}^{(k)}$ functions.

Finally, we take the phase difference $\phi = \theta_2 - \theta_1$, resulting in the scalar equation,

$$\begin{aligned}\dot{\phi} &= \varepsilon [\mathcal{H}(-\phi) - \mathcal{H}(\phi)] \equiv -2\mathcal{H}_{\text{odd}}(\phi) \\ &= \varepsilon \left[\mathcal{H}^{(1)}(-\phi) - \mathcal{H}^{(1)}(\phi) \right] + \varepsilon^2 \left[\mathcal{H}^{(2)}(-\phi) - \mathcal{H}^{(2)}(\phi) \right] \\ &\quad + \varepsilon^3 \left[\mathcal{H}^{(3)}(-\phi) - \mathcal{H}^{(3)}(\phi) \right] + O(\varepsilon^4),\end{aligned}$$

where \mathcal{H}_{odd} is the odd part of \mathcal{H} , and we will often refer to the right-hand side of the above as $-2\mathcal{H}_{\text{odd}}$, or with a slight abuse of notation, simply call them interaction functions. As mentioned earlier, fixed points of the scalar $-2\mathcal{H}_{\text{odd}}$ function inform us of the existence and stability of phase-locked states in a given pair of coupled oscillators. We will demonstrate this property in the examples to follow.

We remark that this expansion is consistent with previously developed strategies for getting the first and second order responses. The first order term contains the functions $M^{(0,0)}$ and $Z^{(0)}$, which are the coupling function G and classic infinitesimal phase response

curve, so $\mathcal{H}^{(1)}$ is the classic interaction function. The second-order term is identical to that derived in [35]. Most importantly, the proposed theory represents an extension of the work in [35] and can be used to calculate coupling functions to arbitrary orders of accuracy in the coupling strength. Higher order approximations are straightforward to attain through symbolic manipulations, which is automated using our Python code.

3 Results

3.1 CGL Model

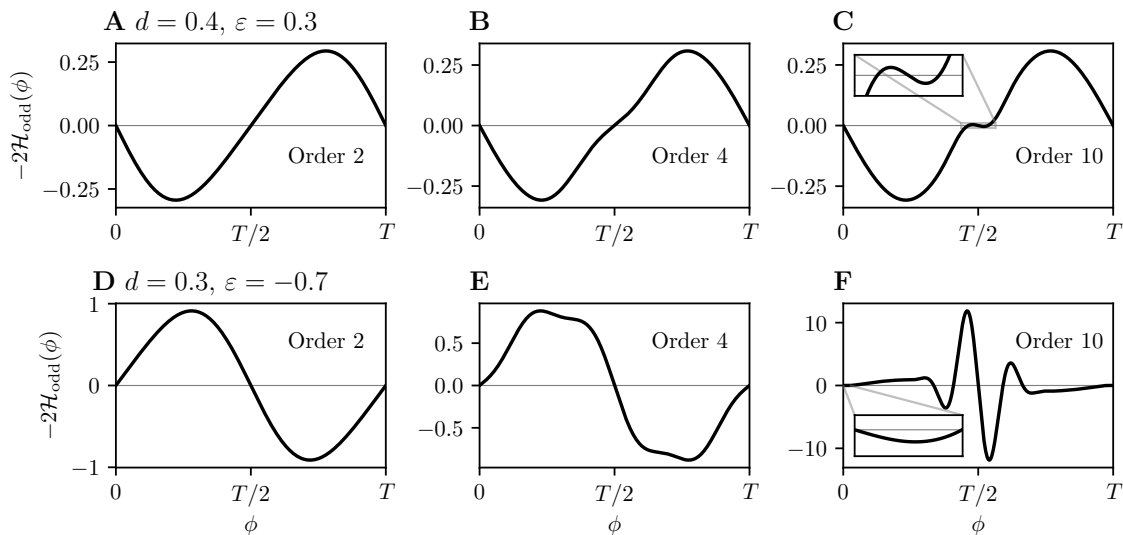


Figure 1: Examples of generalized \mathcal{H} functions in the CGL model. Roots indicate existence of phase-locked solutions (with stability determined by the slopes). A,B,C: second, fourth, and tenth order interaction functions, respectively, for the choice of coupling parameters $d = 0.4$ and $\varepsilon = 0.26$. Stability in the antiphase state only appears in C with the addition of the tenth-order term (inset shows a negative slope at antiphase). D,E,F: higher-order coupling functions for second, fourth, and tenth order, respectively, for the choice of coupling parameters $d = 0.3$ and $\varepsilon = -0.66$. Stability in the synchronous state only appears in F with the addition of the tenth-order term (inset shows a negative slope at synchrony). $q = 1$ for this example.

We begin with a relatively straightforward example of two diffusively coupled complex

Ginzburg-Landau (CGL) models:

$$\begin{aligned}x'_j &= (1 - x_j^2 - y_j^2)x_j - q(x_j^2 + y_j^2)y_j + \varepsilon [x_k - x_j - d(y_k - y_j)], \\y'_j &= (1 - x_j^2 - y_j^2)y_j + q(x_j^2 + y_j^2)x_j + \varepsilon [y_k - y_j + d(x_k - x_j)],\end{aligned}\tag{17}$$

where $j = 3 - k$ with $k = 1, 2$. When $\varepsilon = 0$ and $q = 1$, the system admits a stable 2π -periodic limit cycle, $x_j(t) = \cos(qt)$, $y_j = \sin(qt)$. Depending on the choices of d , q and ε , the model (17) can admit stable phase locked solutions, stable antiphase solutions, or bistability between phase-locked and antiphase solutions. Critical curves that define regions of stability were computed exactly by [1] and are given by

$$\begin{aligned}\varepsilon_s &= \frac{dq - 1}{d^2 + 1}, \\ \varepsilon_a &= \frac{1 - dq}{d^2 - 2dq + 3}.\end{aligned}\tag{18}$$

These curves are shown as black lines in Figure 2 and define regions where different locking modalities are stable. We compare our method to the ground truth of Equation (18) by generating \mathcal{H} functions of different order truncations and tracking the fixed points of the equation

$$\dot{\phi} = \varepsilon [\mathcal{H}(-\phi) - \mathcal{H}(\phi)].$$

as a function of ε and d .

Examples of \mathcal{H} functions are shown in Figure 1. Panels A, B, and C show the \mathcal{H} function for second, fourth, and tenth order for $d = 0.4$ and $\varepsilon = 0.26$. For this coupling strength, second and fourth order \mathcal{H} functions show that antiphase is unstable, but the tenth order function reveals a stable antiphase solution. Panels D, E, F, show the \mathcal{H} function for second, fourth, and tenth order for $d = 0.3$ and $\varepsilon = -0.66$. Second and fourth order show that synchrony is unstable, but the tenth order function reveals a stable synchronous solution.

In Figure 2, we show the boundaries constructed from our theory using second order (purple) and tenth order (green) \mathcal{H} functions. The system switches between stable and unstable synchrony across solid lines (between regions I and III), and between stable and unstable antiphase across dashed lines (between regions I and II). As expected, the tenth-order approximation closely follows the ground-truth curves (black) for a much greater range of d, ε , compared to existing second-order theory. The parameter values corresponding to Figure 1A, B, C are labeled with a star (\star) towards the upper left corner of the diagram. This point is in parameter region I, which corresponds to stable synchrony and unstable antiphase, confirming the accuracy of Figure 1C. The parameter values corresponding to Figure 1D, E, F are labeled with a star (\star) towards the lower left corner of the diagram. This point is also in parameter region I and we confirm stable synchrony and unstable antiphase observed in Figure 1F.

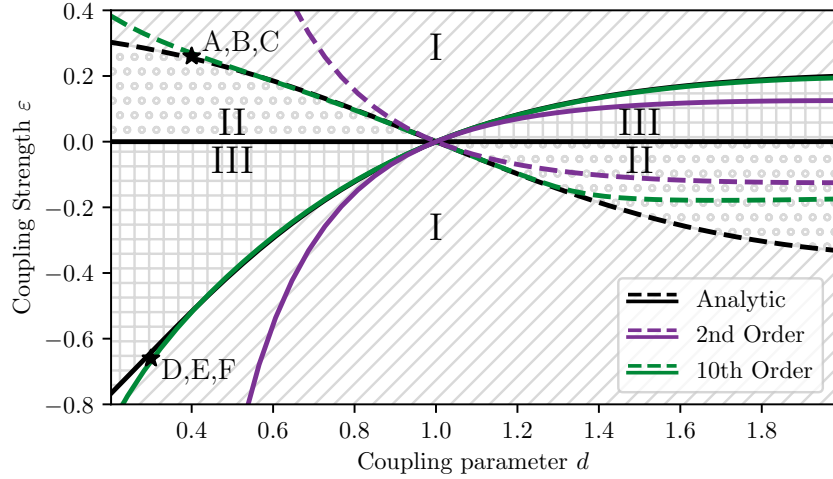


Figure 2: Two-parameter diagram of the CGL model in coupling parameters d and ε . Synchrony is only stable in regions I and II, whereas antiphase is only stable in regions I and III. All black lines are analytically computed from Equation (18). Black solid lines denote boundaries where the system switches between stable and unstable synchrony (ε_s). Black dashed lines denote boundaries where the system switches between stable and unstable antiphase (ε_a). Purple solid, dashed: bifurcations detected using 2nd order interaction functions from [35]. Green solid, dashed: bifurcations detected using 10th order interaction functions. The points labeled $\star A, B, C$ and $\star D, E, F$ correspond to the parameter values used in Figure 1A, B, C, and D, E, F, respectively.

The analytically tractable features of this model allow us to confirm our theory and demonstrate its strong performance. Additionally, our theory can also be applied straightforwardly to analytically intractable models as will be seen in the next example.

3.2 Thalamic Neuron Model

As a second example, we consider a model of synaptically coupled conductance-based neurons taken from [27] that replicate the salient dynamical behaviors of tonically firing

thalamic neurons. The state variables of the thalamic neuron models satisfy

$$\begin{aligned}\frac{dV_i}{dt} &= (-I_L(V_i) + I_{Na}(V_i) + I_K(V_i) + I_T(V_i) - g_{\text{syn}}w_j(V_i - E_{\text{syn}}) + I_{\text{app}})/C, \\ \frac{dh_i}{dt} &= (h_\infty(V_i) - h_i)/\tau_h(V_i), \\ \frac{dr_i}{dt} &= (r_\infty(V_i) - r_i)/\tau_r(V_i), \\ \frac{dw_i}{dt} &= \alpha(1 - w_i)/(1 + \exp((V_i - V_T)/\sigma_T)) - \beta w_i,\end{aligned}$$

where $i = 1, 2$, $j = 3 - i$. The voltage variable V_i depend on the gating variables h_i, r_i , and receives synaptic inputs from the synaptic variable w_j from the reciprocal neuron. We consider excitatory synaptic coupling, $E_{\text{syn}} = 0$. We will use the parameter g_{syn} to denote the coupling strength in this section (it is equivalent to ε in our formulation). All remaining equations are listed in Appendix B along with the parameters in Table A1.

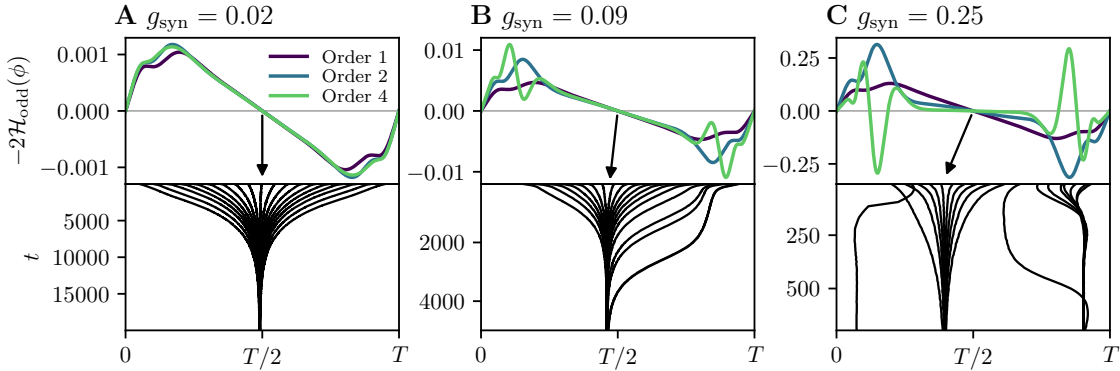


Figure 3: Examples of generalized \mathcal{H} functions in the thalamic model. Roots indicate existence of phase-locked solutions, and slopes the stability. In each top panel, first (purple), second (blue), and fourth (green) order generalized interaction functions are shown. In each bottom panel, the phase difference between two thalamic models are shown for 20 initial conditions. A: with $g_{\text{syn}} = 0.02$, i.e., weak coupling, all orders agree and the full model converges to the antiphase state as indicated by the black arrow. B: with $g_{\text{syn}} = 0.09$, the weak coupling theory remains valid and the stability of fixed points agree with the higher-order interaction functions. However, only the fourth order function captures the slow decay of transients for initial conditions that start near the synchronized solution. C: with $g_{\text{syn}} = 0.25$, only fourth order captures the existence of near-synchronous states. To ease comparisons, we scaled the first order function by a factor of 10 and the second order term by a factor of 7. The black arrow indicates the location of the antiphase point in the full system.

Figure 3 shows generalized \mathcal{H} functions up to first, second, and fourth order for $g_{\text{syn}} \in \{0.01, 0.09, 0.25\}$. For $g_{\text{syn}} = 0.02$, all generalized \mathcal{H} functions exhibit the same types of stability, namely unstable synchrony and stable antiphase (Figure 3A), and the full model converges to antiphase as expected (Figure 3A, black arrow and black curves). For $g_{\text{syn}} = 0.09$, all \mathcal{H} functions agree in stability (Figure 3B, bottom black arrow and black lines). However, only the fourth-order \mathcal{H} function explains the slow transitions to antiphase for solutions near synchrony.

We remark on a few important features in the bottom panels of Figure 3B,C that may appear erroneous but are in fact consistent with our theory. Note that the underlying limit cycle will deform as a function of the coupling strength g_{syn} , and the greater the coupling strength the greater the deformation. Although we don't show the limit cycle deformation explicitly, we have observed that the shape and period of the limit cycle with no coupling, $g_{\text{syn}} = 0$, may differ substantially from the shape and period of the limit cycle for stronger coupling, e.g., when we increase g_{syn} to $g_{\text{syn}} = 0.09$ and $g_{\text{syn}} = 0.25$. In the case of weak coupling, a standard approach is to use the limit cycle with no coupling as a reference point to initialize solutions with some desired phase difference. This choice works well because weak coupling does not perturb solutions far from the unperturbed limit cycle. However, in the case of strong coupling, using the unperturbed limit cycle to initialize solutions results in strong transients as the solutions settle on to the strongly perturbed limit cycle. Because the strongly perturbed limit cycle may differ greatly in shape and period from the unperturbed limit cycle, the transients sometimes allow oscillators to switch in the sign of the phase.

For example, oscillators initialized using the unperturbed limit cycle at θ_1 and θ_2 , where θ_2 lags just behind θ_1 ($\phi = \theta_2 - \theta_1 < 0$), may rapidly switch in order and result in θ_1 lagging just behind θ_2 ($\phi > 0$) as the underlying trajectories settle on to the strongly perturbed limit cycle. It is possible to mitigate the issue of transients by using the strongly perturbed limit cycle as a reference to initialize solutions, but we chose to use the unperturbed limit cycle as it is a standard approach. For the few initial conditions that result in this type of switch, we chose to reverse their sign *post hoc*. For this reason, some initial conditions appear to be missing in Panel B, and some phase difference trajectories overlap in panel C.

Regarding the convergence of phase differences away from the antiphase $T_0/2$ in panels B and C, note that we used the period $T_0 \approx 10.6$ of the unperturbed oscillator to normalize all solutions, so the antiphase state during strong coupling will appear incorrect by a factor of $T_{0.09}/T_0$ and $T_{0.25}/T_0$, where $T_{0.09} \approx 10$ is the period of oscillation at $g_{\text{syn}} = 0.09$ and $T_{0.25} \approx 8.4$ is the period of oscillation at $g_{\text{syn}} = 0.25$. The ratios $T_{0.09}/T_0$ and $T_{0.25}/T_0$ are consistent with the respective differences seen in panels B and C.

We further illustrate the differences between the generalized \mathcal{H} functions using one-parameter bifurcation diagrams (Figure 4). Similar to the CGL model, we follow fixed

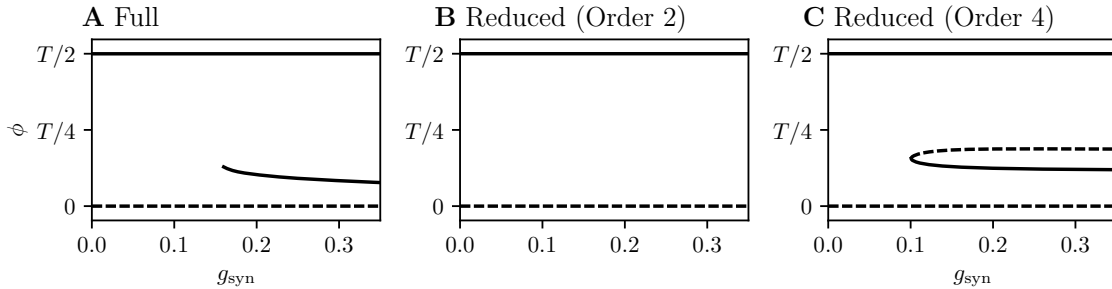


Figure 4: One-parameter bifurcation diagrams in g_{syn} of the phase difference between two Thalamic oscillators. A: Bifurcation diagram of the full system. Synchrony is unstable, antiphase is stable, and for $g_{\text{syn}} \approx 0.15$, a stable near-synchronous state emerges. B: Bifurcation diagram of the reduced system using an order 2 approximation. Synchrony is unstable and antiphase is stable as expected, but there is no near-synchronous solution. The bifurcation diagram when using the order 1 accurate coupling functions (i.e. the standard theory of weakly coupled oscillators) is identical to the order 2 accurate diagram. C: Bifurcation diagram of the reduced system using an order 4 approximation. Synchrony is unstable and antiphase is unstable in agreement with the full model, and the near-synchronous branch appears for $g_{\text{syn}} \approx 0.1$.

points of the phase difference equation

$$\dot{\phi} = g_{\text{syn}} [\mathcal{H}(-\phi) - \mathcal{H}(\phi)],$$

for different order truncations. The bifurcation parameter is naturally g_{syn} .

The one-parameter diagram of the full system exhibits unstable synchrony, stable antiphase, and a stable phase-locked state that emerges at $g_{\text{syn}} \approx 0.15$ as g_{syn} increases (Figure 4A). We are unable to capture unstable phase-locked branches in the full system using XPPAUT [8]. Using the second-order \mathcal{H} function, we capture unstable synchrony and stable antiphase, but we do not capture the stable phase-locked solution. Finally, using the fourth-order \mathcal{H} function, we capture all qualitative features of the full model including the stable phase-locked solution, which emerges at $g_{\text{syn}} \approx 0.1$. We are also able to capture the unstable phase-locked branch.

This result demonstrates the general utility our theory. It is naturally applicable to arbitrary, smooth n -dimensional smooth dynamical systems with arbitrary, smooth coupling functions. Despite stronger coupling inducing relatively large changes to the underlying vector field, the theory robustly reproduces the behaviors of the full, unreduced model.

4 Discussion

In this paper, we have established a general coupled oscillator theory for coupling strengths that extend well beyond the regime of weak coupling. By exploiting phase-amplitude relationships based on the isostable coordinate framework, we derived coupling functions that are valid to arbitrary orders of accuracy in the coupling strength. To verify the theory, we applied our theory to two different models. In the first example, the CGL model, we demonstrated how higher-order coupling functions accurately characterize both the existence and stability of synchronous and antiphase solutions. Using these higher-order coupling functions, we reproduced the analytically derived boundaries in the two-parameter bifurcation diagram with much greater accuracy than existing methods. In the second example, we considered a neurobiologically motivated model of a tonically firing neuron. Our theory accurately reproduced the phase-locked solutions of coupled thalamic models.

Provided relatively mild conditions such as sufficient smoothness of the vector fields are satisfied, our theory can be applied to a wide variety of oscillatory dynamical systems in the biological, chemical, and physical sciences. While we only explicitly considered $N = 2$ oscillators in this paper, an important future direction includes augmenting this theory to networks of oscillators and extending classic results on weakly coupled oscillators.

We have demonstrated the utility of our theory, but some limitations remain. First, strong coupling leads to strongly deformed limit cycles in the full system, and phase information from the weakly coupled system does not necessarily transfer into the strongly coupled system. While our theory is robust to this effect and does not use knowledge of the strongly coupled system, care must be taken when translating from our theory to the full system. The theory is best suited to understanding the *asymptotic* behavior of coupled oscillators (although it is worth reiterating that the theory is capable of reproducing qualitative transient behavior for non-weak coupling).

Other limitations of our theory are computational. Some of the functions in this paper are expensive to compute, but this limitation may be improved by existing work on phase reduction theory for strong perturbations. In [16], the authors introduce the local orthogonal rectification (LOR). In contrast to the isostable framework, LOR codes the amplitude as an orthogonal distance from a limit-cycle trajectory. Other insights that may lead to more efficient computation of coupling functions may be gleaned from [23], where authors introduce a parameterization method to compute higher-order phase-amplitude coordinates, which sidesteps the need to symbolic derivatives and the need to use Newton's method in this work and in [35].

A Numerical Integration

For $N = 2$, our theory requires the computation of the functions

$$p_i^{(k)}(\eta_1, \eta_2) = \int_0^\infty e^{\kappa s} f^{(k)}(\eta_1 - s, \eta_2 - s) ds.$$

The above integral must be repeated for each η_i and η_j , where η_i and η_j are taken from a grid of phase values. If M is the number of discretized points in the interval $[0, T]$, P is the number of discretized points in the interval $(\infty, 0]$, and N is the number of oscillators, then the total number of computations is proportional to $P \times M^N$. This computation is especially expensive if κ is small (requiring large P), or the functions $f^{(k)}$, containing the underlying PRCs, IPRCs, and Floquet eigenfunctions require a fine temporal resolution to integrate (requiring M large). In the case of the thalamic model, κ is small, roughly $\kappa \approx 0.023$, and at least 20000 time units were required to compute the PRC, IRC, and Floquet eigenfunctions to acceptable accuracy (in contrast, the CGL model required 2000 time units). We used $P = 25 \times M$, so each integral calculation was relatively costly. We found that the η_i and η_j was best sampled using $M = 4000$, i.e., a grid of 4000×4000 discretized phase values, so the integral was computed 16 million times. We found Riemann integration to be efficient and sufficiently accurate.

To speed up computations of the above integral, we transformed it to minimize repeating calculations in two variables. Letting $u = \eta_1 - s$, a straightforward transformation yields

$$e^{\kappa \eta_1} \left[\int_{-\infty}^0 e^{-\kappa u} f(u, \eta_2 - \eta_1 + u) du + \int_0^{\eta_1} e^{-\kappa u} f(u, \eta_2 - \eta_1 + u) du \right].$$

Note that the first integral depends only on the phase difference $\eta_2 - \eta_1$, so it is computed along only one dimension, and the total number of computations is proportional to $P \times M \times (N - 1)$. The second integral does not solely depend on the phase difference $\eta_2 - \eta_1$, and must be computed in two dimensions. However, the computation is not on the entire grid of η_1, η_2 points, but on a triangular half of the domain because the upper integral limit varies as a function of η_1 . The number of computations for the second integral is proportional to $M^N/2$. The total number of calculations $P \times M \times (N - 1) + M^N/2$, which is a significant reduction compared to the original integral.

Finally, we vectorized and computed each integral independently for any given η_1, η_2 , allowing us to parallelize the integral computation. The parallelization uses the `pathos` multiprocessing module to allow more robust serialization, and not the standard `multiprocessing` module. Assuming that the PRC, IRPC, and Floquet eigenfunctions have been computed, solving for $p_i^{(k)}$ up to order 4 with $M = 4000$ takes approximately 45 minutes for the thalamic model on 8 cores. Solving $p_i^{(k)}$ for the CGL model only requires $M = 200$ and takes roughly 5-10 minutes on two cores.

Table A1: Thalamic model parameter values

Parameter	Value
C	$1\mu\text{F}/\text{cm}^2$
E_k	-90mV
E_{Na}	50mV
E_t	0mV
E_l	-70mV
E_{syn}	0mV
g_l	$0.05\text{mS}/\text{cm}^2$
g_k	$5\text{mS}/\text{cm}^2$
g_{Na}	$3\text{mS}/\text{cm}^2$
g_{syn}	$0 - 0.25\text{mS}/\text{cm}^2$
α	3
β	2
σ_T	0.8
V_T	-20mV
I_{app}	$3.5\mu\text{A}/\text{cm}^2$

B Thalamic Model

The remaining equations for the Thalamic model are

$$I_L(V) = g_L(V - E_L), \quad I_{Na} = g_{Na} h m_\infty^3(V)(V - E_{Na}),$$

$$I_K = 0.75 g_K (1 - h)^4 (V - E_K), \quad I_T = g_T r p_\infty^2(V)(V - E_T),$$

and

$$a_h(V) = 0.128 \exp(-(V + 46)/18), \quad b_h(V) = 4/(1 + \exp(-(V + 23)/5)),$$

$$m_\infty(V) = 1/(1 + \exp(-(V + 37)/7)), \quad h_\infty(V) = 1/(1 + \exp((V + 41)/4)),$$

$$r_\infty(V) = 1/(1 + \exp((V + 84)/4)), \quad p_\infty(V) = 1/(1 + \exp(-(V + 60)/6.2)),$$

$$\tau_h(V) = 1/(a_h(V) + b_h(V)), \quad \tau_r(V) = 28 + \exp(-(V + 25)/10.5).$$

Please see Table A1 for the parameters.

Acknowledgments

The authors acknowledge support under National Institute of Health grant T32 NS007292 (YP) and National Science Foundation Grant No. CMMI-1933583 (DW).

References

- [1] Donald G Aronson, G Bard Ermentrout, and Nancy Kopell. Amplitude response of coupled oscillators. *Physica D: Nonlinear Phenomena*, 41(3):403–449, 1990.
- [2] Marko Budišić, Ryan Mohr, and Igor Mezić. Applied Koopmanism. *Chaos: An Interdisciplinary Journal of Nonlinear Science*, 22(4):047510, 2012.
- [3] Robert J Butera Jr, John Rinzel, and Jeffrey C Smith. Models of respiratory rhythm generation in the pre-bötzinger complex. ii. populations of coupled pacemaker neurons. *Journal of neurophysiology*, 82(1):398–415, 1999.
- [4] Florian Dörfler, Michael Chertkov, and Francesco Bullo. Synchronization in complex oscillator networks and smart grids. *Proc. Natl. Acad. Sci. USA*, 110(6):2005–2010, 2013.
- [5] Irving R Epstein and John A Pojman. *An introduction to nonlinear chemical dynamics: oscillations, waves, patterns, and chaos*. Oxford University Press, 1998.
- [6] Bard Ermentrout, Youngmin Park, and Dan Wilson. Recent advances in coupled oscillator theory. *Philos. Trans. Roy. Soc. A*, 377(2160):20190092, 16, 2019.
- [7] G. Bard Ermentrout. $n : m$ phase-locking of weakly coupled oscillators. *J. Math. Biol.*, 12(3):327–342, 1981.
- [8] G. Bard Ermentrout. *Simulating, analyzing, and animating dynamical systems: a guide to XPPAUT for researchers and students*, volume 14. SIAM, 2002.
- [9] G. Bard Ermentrout and David H. Terman. *Mathematical foundations of neuroscience*, volume 35 of *Interdisciplinary Applied Mathematics*. Springer, New York, 2010.
- [10] George Bard Ermentrout and Nancy Kopell. Frequency plateaus in a chain of weakly coupled oscillators. I. *SIAM J. Math. Anal.*, 15(2):215–237, 1984.
- [11] Erik Genge, Erik Teichmann, Michael Rosenblum, and Arkady Pikovsky. High-order phase reduction for coupled oscillators. *arXiv preprint arXiv:2007.14077*, 2020.
- [12] Jorge Golowasch, Frank Buchholtz, Irving R Epstein, and E Marder. Contribution of individual ionic currents to activity of a model stomatogastric ganglion neuron. *Journal of Neurophysiology*, 67(2):341–349, 1992.
- [13] Frank C. Hoppensteadt and Eugene M. Izhikevich. *Weakly connected neural networks*, volume 126 of *Applied Mathematical Sciences*. Springer-Verlag, New York, 1997.
- [14] Eugene M. Izhikevich. *Dynamical systems in neuroscience: the geometry of excitability and bursting*. Computational Neuroscience. MIT Press, Cambridge, MA, 2007.

- [15] Y. Kuramoto. *Chemical oscillations, waves, and turbulence*, volume 19 of *Springer Series in Synergetics*. Springer-Verlag, Berlin, 1984.
- [16] Benjamin Letson and Jonathan E Rubin. LOR for analysis of periodic dynamics: A one-stop shop approach. *SIAM Journal on Applied Dynamical Systems*, 19(1):58–84, 2020.
- [17] Jan R Magnus and Heinz Neudecker. *Matrix differential calculus with applications in statistics and econometrics*. John Wiley & Sons, 2019.
- [18] Alexandre Mauroy, Igor Mezić, and Jeff Moehlis. Isostables, isochrons, and Koopman spectrum for the action–angle representation of stable fixed point dynamics. *Physica D: Nonlinear Phenomena*, 261:19–30, 2013.
- [19] Igor Mezić. Analysis of fluid flows via spectral properties of the Koopman operator. *Annual Review of Fluid Mechanics*, 45:357–378, 2013.
- [20] Edward Ott and Thomas M Antonsen. Low dimensional behavior of large systems of globally coupled oscillators. *Chaos: An Interdisciplinary Journal of Nonlinear Science*, 18(3):037113, 2008.
- [21] Youngmin Park and Bard Ermentrout. Weakly coupled oscillators in a slowly varying world. *J. Comput. Neurosci.*, 40(3):269–281, 2016.
- [22] Youngmin Park, Stewart Heitmann, and G. Bard Ermentrout. The utility of phase models in studying neural synchronization. *Computational Models of Brain and Behavior*, pages 493–504, 2017.
- [23] Alberto Pérez-Cervera, Tere M Seara, and Gemma Huguet. Global phase-amplitude description of oscillatory dynamics via the parameterization method. *arXiv preprint arXiv:2004.03647*, 2020.
- [24] Carsten K Pfeffer, Mingshan Xue, Miao He, Z Josh Huang, and Massimo Scanziani. Inhibition of inhibition in visual cortex: the logic of connections between molecularly distinct interneurons. *Nature Neuroscience*, 16(8):1068–1076, 2013.
- [25] Anastasiya V Pimenova, Denis S Goldobin, Michael Rosenblum, and Arkady Pikovsky. Interplay of coupling and common noise at the transition to synchrony in oscillator populations. *Scientific Reports*, 6:38518, 2016.
- [26] Michael Rosenblum and Arkady Pikovsky. Numerical phase reduction beyond the first order approximation. *Chaos: An Interdisciplinary Journal of Nonlinear Science*, 29(1):011105, 2019.

- [27] Jonathan E Rubin and David Terman. High frequency stimulation of the subthalamic nucleus eliminates pathological thalamic rhythmicity in a computational model. *Journal of Computational Neuroscience*, 16(3):211–235, 2004.
- [28] Michael A Schwemmer and Timothy J Lewis. The theory of weakly coupled oscillators. In *Phase Response Curves in Neuroscience*, pages 3–31. Springer, 2012.
- [29] Steven H Strogatz, Daniel M Abrams, Allan McRobie, Bruno Eckhardt, and Edward Ott. Crowd synchrony on the millennium bridge. *Nature*, 438(7064):43–44, 2005.
- [30] Corey Michael Thibeault and Narayan Srinivasa. Using a hybrid neuron in physiologically inspired models of the basal ganglia. *Frontiers in Computational Neuroscience*, 7:88, 2013.
- [31] Guido Van Rossum and Fred L Drake Jr. *Python reference manual*. Centrum voor Wiskunde en Informatica Amsterdam, 1995.
- [32] Dan Wilson. Phase-amplitude reduction far beyond the weakly perturbed paradigm. *Physical Review E*, 101(2):022220, 2020.
- [33] Dan Wilson and Bard Ermentrout. Greater accuracy and broadened applicability of phase reduction using isostable coordinates. *J. Math. Biol.*, 76(1-2):37–66, 2018.
- [34] Dan Wilson and Bard Ermentrout. Augmented phase reduction of (not so) weakly perturbed coupled oscillators. *SIAM Review*, 61(2):277–315, 2019.
- [35] Dan Wilson and Bard Ermentrout. Phase models beyond weak coupling. *Physical Review Letters*, 123(16):164101, 2019.
- [36] Dan Wilson and Jeff Moehlis. Isostable reduction of periodic orbits. *Physical Review E*, 94(5):052213, 2016.
- [37] Arthur T Winfree. *The geometry of biological time*, volume 12. Springer Science & Business Media, 2001.